# Geoengineering: Whiter Skies?

# (Supplemental Online Material)

Ben Kravitz,[1*] Douglas G. MacMartin,[2] Ken Caldeira[1]

[1]Department of Global Ecology, Carnegie Institution for Science,

260 Panama Street, Stanford, CA 94305, USA

[2]Department of Control and Dynamical Systems, California Institute of Technology,

1200 E. California Blvd., Pasadena, CA 91125, USA

[*]Corresponding author; E-mail: bkravitz@carnegie.stanford.edu.

## 1 Model

To perform our simulations, we used the libRadtran software package, version 1.6$\beta$ (*1, 2, 3*). We used two components from this model package: `mie` and `uvspec`. The `mie` component calculates scattering properties of aerosols, which are then provided as input for `uvspec`, which is the core radiative transfer tool.

For the aerosol scattering properties, we use the Mie code `MIEV0` (*4*). We specify that 200 moments of the scattering phase function be calculated, which, for the experiments we

have performed, is more than sufficient for convergence of the summed terms of the phase function. Scattering is calculated in the entire visible spectrum, from 380 to 780 nm, with a wavelength step of 1 nm. Since we are simulating sulfate aerosols, we have specified the complex refractive index for the aerosols to be $1.43 + 0i$. For an aerosol composition of 75% $H_2SO_4$ and 25% water, which is typical for sulfate aerosols (*5*), this refractive index is valid for the range of wavelengths we investigate (*6, 7*). Linearly interpolating from the values given in (*6*), the range of refractive indices over this set of wavelengths varies from $1.428 + 0i$ to $1.446 + 0i$, which is a small enough variation from the assumed value of $1.43 + 0i$ that our results are not affected. The Mie code outputs aerosol extinction, single scattering albedo, and the moments of the scattering phase function for each wavelength, based on the assumed size distribution (discussed in the following sections), which are then provided as input to the radiative transfer code `uvspec`.

`uvspec` is designed to calculate spectral irradiance in ultraviolet and visible wavelengths (*3, 8*). Our specifications are for a standard atmospheric temperature and gas profile in the summer over the continental United States. We use the DISORT algorithm (*9*) to calculate irradiance over the visible spectrum 380-780 nm at 1 nm intervals. All radiative transfer simulations were calculated at a reference height of 0.0 km and with a solar zenith angle of 0°, except where indicated (Section 3 and Figure 1).

# 2 Geoengineering

For our geoengineering simulations, we began with Mie code simulations of unimodal lognormal distributions of sulfate aerosols with median radii of $r_g = \{0.1, 0.2, 0.3, 0.4, 0.5, 0.6, 0.7, 0.8, 0.9\}$ $\mu$m and standard deviations of $\sigma = \{0.1, 0.25, 0.5, 1.0\}$, for a total of 36 simulations. The output from the Mie code simulations was provided as input to `uvspec` with a prescribed

aerosol optical depth (mid-visible, $\lambda = 550$ nm) of 0.1. We then integrated spectral irradiance over the visible spectrum and calculated the appropriate mid-visible optical depth required to scale that integrated value to achieve a reduction by 0.5, 1.0, 1.5, and 2.0%. Optical depths at all other wavelengths are scaled appropriately according to the extinction efficiencies calculated by the Mie code. These mid-visible optical depths can be found in Supplementary Table 2. The radiative transfer simulations were then redone with these updated optical depth values for a total of 144 simulations.

Although all of our calculations are specified in terms of a percent decrease in solar irradiance, this is calculated by integrating spectral irradiance only over the visible spectrum ($\lambda = 380 - 780$ nm) instead of the total solar band. The visible band accounts for approximately 52% of the energy in the solar spectrum, with approximately 3% occurring in the ultraviolet (UV) portion and 45% in the near infrared (NIR) portion of the spectrum (*10*). Moreover, sulfate aerosol extinction in the NIR band is approximately one order of magnitude less than in the visible and UV bands (*11*). Naively calculating integrated irradiance values using these values, a 2% reduction in visible integrated spectral irradiance is the same as a 1.19% reduction in total integrated spectral irradiance, which seemingly implies our geoengineering simulations understate changes in sky color. However, these values are based on the assumption that the shape of the spectral irradiance curve does not change in the NIR, which, based on extrapolations of Figure 2, is not likely to be true in general.

We cannot resolve this uncertainty in spectral irradiance changes in the NIR. Narrow absorption lines in the NIR necessitate the use of a correlated-$k$ distribution in conducting radiative transfer simulations, which does not allow for the fine spectral resolution we have obtained in our simulations of visible spectral irradiance. Therefore, we have decided not to pursue this route and to frame our geoengineering simulations in terms of reductions in

solar irradiance integrated over the visible band.

# 3 Mount Pinatubo simulation

One additional simulation we conducted was for the 1991 eruption of Mount Pinatubo as a comparison to our geoengineering and pollution (Section S5 below) simulations. The simulation with `mie` involved a lognormal distribution with specified effective radius of $r_{\text{eff}} = 0.5248$ $\mu$m and $\sigma_g = 1.4$, which corresponds to approximate values in March 1992, 9 months after the eruption (*12, 13, 14*). As in the geoengineering simulations, we used a complex refractive index of $1.43 + 0i$. Our simulation with `uvspec` used a mid-visible aerosol optical depth of $\tau_{550} = 0.12$, which was the value measured at the Mauna Loa Observatory (19.5°N, 155.6°W) in March 1992 (*12*). At this time, the eruption showed approximately a 20% decrease in direct radiation, which was compensated by a 240% increase in diffuse radiation at solar zenith angle 60° (*13*). Results of our simulations of these conditions are within 4% of these values.

# 4 Thin Cirrus

To account for the potential effects of optically thin cirrus clouds on our results, we performed simulations including cirrus clouds. We chose typical values of cirrus clouds: cloud fraction 20%, cloud droplet effective radius 20 $\mu$m, and ice water content of 0.005 g m$^{-3}$ (*15*). We inserted these clouds into a layer at 10 km in altitude, below the layer of stratospheric aerosols. Irradiance results for these simulations, assuming a geoengineering aerosol size distribution with $r_g$=0.5 $\mu$m and $\sigma = 0.1$, are in Supplementary Figure 1. Iincreases in sky brightness as a function of the size distribution are in Supplementary Table 3.

# 5 Pollution

For our comparisons in Figure 4, we obtained aerosol optical depth and size distribution data for several urban centers (*16*) and averaged the values, weighted by the number of observations at each site. All of these parameters had a range, corresponding to days with low, high, and average aerosol conditions, which depended upon meteorology. Additionally, each site had a range of Angstrom exponents, which we incorporated into the simulations. All values we used for our simulations can be found in Supplementary Table 1.

To perform our simulations, we generated bimodal distributions which we inserted into `mie`, one for each combination of low, high, and average aerosol. We then provided this as input for `uvspec`, each of which had three choices of Angstrom exponent (low end of the range, high end of the range, and the average value in the range), for a total of 9 simulations. These results are shown in Figure 4, in which the average condition is shown as a solid colored line, and the range spanned by choosing different Angstrom exponents is shown as colored shading. For the `uvspec` simulations, we assumed the background aerosol profile to be urban spring/summer, with background stratospheric aerosols, i.e., no recent volcanic eruptions (*17* for further description).

# 6 Metameric Matches

To determine metameric matches for the spectra we generated, we follow a matching procedure (*18*). Eye cones can be divided into three categories, corresponding to the wavelengths to which they are sensitive: short (S), middle (M), and long (L). Supplementary Figure 2 shows each of the cone sensitivities as a function of wavelength, calculated for an average observer (*19*). Using these in combination with our radiative transfer simulations, we can

determine the unsaturated monochromatic stimulus response ($\lambda_u$) that is a metameric match for the simulated sky color by solving the equivalence

$$\frac{M(\lambda_u)\int L(\lambda)I(\lambda)\,d\lambda - L(\lambda_u)\int M(\lambda)I(\lambda)\,d\lambda}{\int L(\lambda)\,d\lambda\int M(\lambda)I(\lambda)\,d\lambda - \int M(\lambda)\,d\lambda\int L(\lambda)I(\lambda)\,d\lambda} \tag{1}$$

$$= \frac{M(\lambda_u)\int S(\lambda)I(\lambda)\,d\lambda - S(\lambda_u)\int M(\lambda)I(\lambda)\,d\lambda}{\int S(\lambda)\,d\lambda\int M(\lambda)I(\lambda)\,d\lambda - \int M(\lambda)\,d\lambda\int S(\lambda)I(\lambda)\,d\lambda}$$

where S, M, and L are the cone spectral sensitivities for the three cone types as a function of wavelength (Supplementary Figure 2), and $I(\lambda)$ is the diffuse spectral irradiance from the radiative transfer simulations. Values of $\lambda_u$ lie at intersections of the curves corresponding to the left and right sides of the equation. Corresponding function values (either side of the above equation) evaluated at $\lambda_u$ are the ratios $I_w/I_u$, which is the relative amounts of white (numerator) and monochromatic light (denominator) of the metameric match, where white light is defined as having equal intensity at all wavelengths. The results of these matches can be found in Figure 3.

# 7 Attempted Visualizations: Color Swatches

As discussed in Section 4, color is not an intrinsic property of light, making visualization of sky color rather difficult. Color perception depends upon biology, including expectations of color, but also upon the color matching function chosen to map the spectrum into RGB space, as well as the assumed white point. To illustrate the dependence of color swatches upon the color matching function and white point, Supplementary Figures 3-6 show combinations of two different choices of each, all of which are reasonable and defensible choices (*20,21,22*). Additionally, the RGB color space is device-dependent, in that different colors can be realized

on different monitors, printers, or any other means of viewing. Therefore, we have no reliable way of ensuring the swatches as viewed on our computer monitors/printers will match those of any reader of this paper. We are satisfied that the only way to represent absolute color is to provide the full visible irradiance spectrum.

# References


1. Mayer, B. Seckmeyer, G. Kylling, A. Systematic long-term comparison of spectral UV measurements and UVSPEC modeling results. *J. Geophys. Res.* **102,** 8755-8767 (1997), doi:10.1029/97JD00240.

2. Mayer, B. Kylling, A. Madronich, S. Seckmeyer, G. Enhanced absorption of UV radiation due to multiple scattering in clouds: Experimental evidence and theoretical explanation. *J. Geophys. Res.* **103,** 31241-31254 (1998), doi:10.1029/98JD02676.

3. Mayer, B. Kylling, A. Technical note: The libRadtran software package for radiative transfer calculations–description and examples of use. *Atmos. Chem. Phys.* **5,** 1855-1857 (2005), doi:10.5194/acp-5-1855-2005.

4. Wiscombe, W. J. Improved Mie scattering algorithms. *Appl. Opt.* **19**, 1505-1509 (1980), doi:10.1364/AO.19.001505.

5. Rosen, J. M. The boiling point of stratospheric aerosols. *J. Appl. Meteor.* **10,** 1044-1046 (1971), doi:10.1175/1520-0450(1971)010<1044:TBPOSA>2.0.CO;2.

6. Palmer, K. F. Williams, D. Optical constants of sulfuric acid; Application to the clouds of Venus? *Appl. Opt.* **14,** 208-219 (1975), doi:10.1364/AO.14.000208.

7. Tang, I. N. Munkelwitz, H. R. Simultaneous determination of refractive index and density of an evaporating aqueous solution droplet. *Aer. Sci. Tech.* **15,** 201-207 (1991), doi:10.1080/02786829108959527.

8. Kylling, A. Stamnes, K. Efficient yet accurate solution of the linear transport equation in the presence of internal sources: The exponential-linear-in-depth approximation. *J. Com. Phys.* **102,** 265-276 (1992).

9. Stamnes, K. Tsay, S.-C.Wiscombe, W. Jayaweera, K. Numerically stable algorithm for discrete-ordinate-method radiative transfer in multiple scattering and emitting layered media. *Appl. Opt.* **27,** 2502-2509 (1988).

10. Yamasaki, R. S. Intensity variations of ultraviolet, visible, and near infrared bands of terrestrial solar radiation. *J. Paint Tech.* **43,** 75-83 (1971).

11. Hess, M. Koepke, P. Schult, I. Optical properties of aerosols and clouds: The software package OPAC. *Bull. Amer. Met. Soc.* **79,** 831-844 (1998).

12. Russell, P. B. *et al.* Global to microscale evolution of the Pinatubo volcanic aerosol derived from diverse measurements and analyses. *J. Geophys. Res.* **101,** 18745-18763 (1996), doi:10.1029/96JD01162.

13. Dutton, E. G. Christy, J. R. Solar radiative forcing at selected locations and evidence for global lower tropospheric cooling following the eruptions of El Chichòn and Pinatubo. *Geophys. Res. Lett.* **19,** 2313-2316 (1992).

14. Del Guasta, M. Morandi, M. Stefanutti, L. Stein, B. Wolf, J. P. Derivation of Mount Pinatubo stratospheric aerosol mean size distribution by means of a multiwavelength lidar. *Appl. Opt.* **33,** 5690-5697 (1994).

158 15. Mace, G. G., E. E. Clothiaux, and T. P. Ackerman (2001), The composite character-
159 istics of cirrus clouds: Bulk properties revealed by one year of continuous cloud data,
160 *J. Clim.*, *14*, 2185-2203.

161 16. Dubovik, O. *et al.* Variability of absorption and optical properties of key aerosol types
162 observed in worldwide locations. *J. Atmos. Sci.* **59,** 590-608 (2002).

163 17. Shettle, E. "Models of aerosols, clouds and precipitation for atmospheric propagation
164 studies," *Atmospheric propagation in the uv, visible, ir and mm-region and related*
165 *system aspects, AGARD Conference Proceedings No. 454* (1989).

166 18. Smith, G. S. Human color vision and the unsaturated blue color of the daytime sky.
167 *Am. J. Phys.* **73,** 590-597 (2005), doi:10.1119/1.1858479.

168 19. Stockman, A. Sharpe, L. T. The spectral sensitivites of the middle and long-wavelength-
169 sensitive cones derived from measurements in observers of known genotype. *Vision Res.*
170 **40,** 1711-1737 (2000).

171 20. Wyszecki, G. Proposal for a New Color-Difference Formula. *J. Opt. Soc. Am.* **53,**
172 1318-1319 (1963), doi:10.1364/JOSA.53.001318.

173 21. Ohta, E. N. Robertson, A. R. *Colorimetry: Fundamentals and Applications* (Wiley,
174 New York, 2006).

175 22. Stiles, W. S. Burch, J. M. N. P. L. Colour-matching investigation: Final Report. *Optica*
176 *Acta* **6,** 1-26 (1959), doi:10.1080/713826267.

Table 1: Specifications for urban aerosols used in Sections 5 and S5. All values are averages (16), weighted by the number of observations at each site. Since values were given as ranges, we have created multiple profiles, based on low, average, and high aerosol amounts. The urban/mixed aerosol profiles we obtained had average refractive indices of $1.43 + 0.01i$, but in our simulations of urban environments, we set these values to $1.43 + 0i$ and 1.00, which are typical for pure sulfate aerosols (*6,7*). The impacts of this assumption on simulated irradiance spectra are quite small, and it has the benefit of making the urban aerosol profiles directly comparable to our geoengineering simulations. All size distributions are assumed to be bimodal lognormal. Concentrations are relative between the two modes (only the shapes of the distribution curves are important, not the values), so units are not given.

| Parameter | Description | Low | Average | High |
|---|---|---|---|---|
| $\tau_{440}$ | Aerosol optical depth (440 nm) | 0.1 | 0.3 | 1.2 |
| $\alpha$ | Angstrom exponent | 1.0-2.4 | 1.0-2.4 | 1.0-2.4 |
| $n + ik$ | Complex refractive index | $1.43 + 0i$ | $1.43 + 0i$ | $1.43 + 0i$ |
| $\omega_{0,440}$ | Single scattering albedo (440 nm) | 1.0 | 1.0 | 1.0 |
| $r_{g_1}$ | Median radius, fine mode ($\mu$m) | 0.13 | 0.17 | 0.21 |
| $\sigma_1$ | Standard deviation, fine mode | 0.41 | 0.41 | 0.41 |
| $C_1$ | Aerosol concentration, fine mode | 0.014 | 0.0865 | 0.159 |
| $r_{g_2}$ | Median radius, coarse mode ($\mu$m) | 2.91 | 3.215 | 3.52 |
| $\sigma_2$ | Standard deviation, coarse mode | 0.72 | 0.72 | 0.72 |
| $C_2$ | Aerosol concentration, coarse mode | 0.013 | 0.058 | 0.103 |

Table 2: Values of aerosol optical depth at 550 nm used in the radiative transfer calculations to achieve the given percent reduction in integrated visible band irradiance reaching the surface ($\Delta I$). The procedure for obtaining these is given in Section S2. $r_g$ is the geometric mean radius, or the median radius, of the assumed unimodal lognormal distribution.

| $r_g$ ($\mu$m) | $\Delta I$ (%) | $\sigma = 0.1$ | $\sigma = 0.25$ | $\sigma = 0.5$ | $\sigma = 1.0$ |
|---|---|---|---|---|---|
| 0.1 | 0.5 | 0.0696 | 0.0631 | 0.0687 | 0.0775 |
| | 1.0 | 0.1396 | 0.1265 | 0.1377 | 0.1554 |
| | 1.5 | 0.2099 | 0.1902 | 0.2071 | 0.2336 |
| | 2.0 | 0.2806 | 0.2543 | 0.2768 | 0.3123 |
| 0.2 | 0.5 | 0.0793 | 0.0624 | 0.0670 | 0.0778 |
| | 1.0 | 0.1591 | 0.1251 | 0.1343 | 0.1560 |
| | 1.5 | 0.2392 | 0.1881 | 0.2020 | 0.2346 |
| | 2.0 | 0.3198 | 0.2514 | 0.2700 | 0.3136 |
| 0.3 | 0.5 | 0.0817 | 0.0610 | 0.0653 | 0.0774 |
| | 1.0 | 0.1637 | 0.1224 | 0.1310 | 0.1553 |
| | 1.5 | 0.2462 | 0.1841 | 0.1970 | 0.2335 |
| | 2.0 | 0.3291 | 0.2460 | 0.2633 | 0.3122 |
| 0.4 | 0.5 | 0.0743 | 0.0585 | 0.0638 | 0.0770 |
| | 1.0 | 0.1490 | 0.1172 | 0.1280 | 0.1544 |
| | 1.5 | 0.2240 | 0.1763 | 0.1924 | 0.2322 |
| | 2.0 | 0.2995 | 0.2357 | 0.2572 | 0.3104 |
| 0.5 | 0.5 | 0.0612 | 0.0550 | 0.0626 | 0.0766 |
| | 1.0 | 0.1228 | 0.1103 | 0.1254 | 0.1536 |
| | 1.5 | 0.1846 | 0.1659 | 0.1886 | 0.2309 |
| | 2.0 | 0.2468 | 0.2218 | 0.2521 | 0.3087 |
| 0.6 | 0.5 | 0.0475 | 0.0517 | 0.0616 | 0.0763 |
| | 1.0 | 0.0953 | 0.1037 | 0.1236 | 0.1530 |
| | 1.5 | 0.1433 | 0.1560 | 0.1858 | 0.2300 |
| | 2.0 | 0.1916 | 0.2085 | 0.2484 | 0.3075 |
| 0.7 | 0.5 | 0.0388 | 0.0498 | 0.0612 | 0.0761 |
| | 1.0 | 0.0777 | 0.0998 | 0.1226 | 0.1527 |
| | 1.5 | 0.1169 | 0.1501 | 0.1844 | 0.2296 |
| | 2.0 | 0.1562 | 0.2006 | 0.2465 | 0.3069 |
| 0.8 | 0.5 | 0.0384 | 0.0499 | 0.0613 | 0.0762 |
| | 1.0 | 0.0769 | 0.1000 | 0.1228 | 0.1527 |
| | 1.5 | 0.1157 | 0.1504 | 0.1847 | 0.2296 |
| | 2.0 | 0.1546 | 0.2011 | 0.2469 | 0.3070 |
| 0.9 | 0.5 | 0.0457 | 0.0521 | 0.0619 | 0.0764 |
| | 1.0 | 0.0916 | 0.1045 | 0.1242 | 0.1531 |
| | 1.5 | 0.1377 | 0.1572 | 0.1868 | 0.2302 |
| | 2.0 | 0.1841 | 0.2101 | 0.2496 | 0.3078 |

Table 3: Increases in visible band integrated diffuse irradiance as a measure of diffuse sky brightness with inclusion of the effects of cirrus clouds (description in Section S4). Leftmost column indicates the percent decrease in total integrated visible band irradiance. All values given are ratios of integrated visible band irradiance (geoengineering divided by clear sky) and are rounded to two decimal places. In the clear sky simulations, diffuse irradiance comprises approximately 6% of total irradiance.

| $\Delta I$ (%) | $\sigma$ | $r_g$ ($\mu$m) | | | | | | | | |
|---|---|---|---|---|---|---|---|---|---|---|
| | | 0.1 | 0.2 | 0.3 | 0.4 | 0.5 | 0.6 | 0.7 | 0.8 | 0.9 |
| 0.5 | 0.1 | 1.44 | 1.50 | 1.51 | 1.47 | 1.40 | 1.33 | 1.30 | 1.28 | 1.29 |
| | 0.25 | 1.43 | 1.41 | 1.40 | 1.39 | 1.37 | 1.35 | 1.33 | 1.33 | 1.34 |
| | 0.5 | 1.46 | 1.44 | 1.43 | 1.42 | 1.42 | 1.41 | 1.41 | 1.41 | 1.41 |
| | 1.0 | 1.52 | 1.52 | 1.52 | 1.51 | 1.51 | 1.51 | 1.51 | 1.51 | 1.51 |
| 1.0 | 0.1 | 1.86 | 1.96 | 1.98 | 1.91 | 1.78 | 1.65 | 1.57 | 1.54 | 1.57 |
| | 0.25 | 1.80 | 1.79 | 1.77 | 1.75 | 1.71 | 1.67 | 1.64 | 1.64 | 1.66 |
| | 0.5 | 1.88 | 1.86 | 1.84 | 1.82 | 1.80 | 1.79 | 1.79 | 1.79 | 1.80 |
| | 1.0 | 1.99 | 2.00 | 1.99 | 1.99 | 1.98 | 1.98 | 1.98 | 1.98 | 1.98 |
| 1.5 | 0.1 | 2.24 | 2.39 | 2.42 | 2.31 | 2.13 | 1.95 | 1.83 | 1.80 | 1.83 |
| | 0.25 | 2.16 | 2.14 | 2.12 | 2.08 | 2.03 | 1.98 | 1.94 | 1.94 | 1.96 |
| | 0.5 | 2.27 | 2.23 | 2.21 | 2.19 | 2.16 | 2.15 | 2.14 | 2.14 | 2.15 |
| | 1.0 | 2.43 | 2.44 | 2.43 | 2.42 | 2.42 | 2.41 | 2.41 | 2.41 | 2.41 |
| 2.0 | 0.1 | 2.59 | 2.77 | 2.82 | 2.68 | 2.45 | 2.23 | 2.08 | 2.04 | 2.08 |
| | 0.25 | 2.50 | 2.48 | 2.45 | 2.40 | 2.34 | 2.27 | 2.23 | 2.22 | 2.25 |
| | 0.5 | 2.63 | 2.60 | 2.56 | 2.53 | 2.50 | 2.48 | 2.47 | 2.48 | 2.49 |
| | 1.0 | 2.83 | 2.84 | 2.83 | 2.82 | 2.82 | 2.81 | 2.81 | 2.81 | 2.81 |

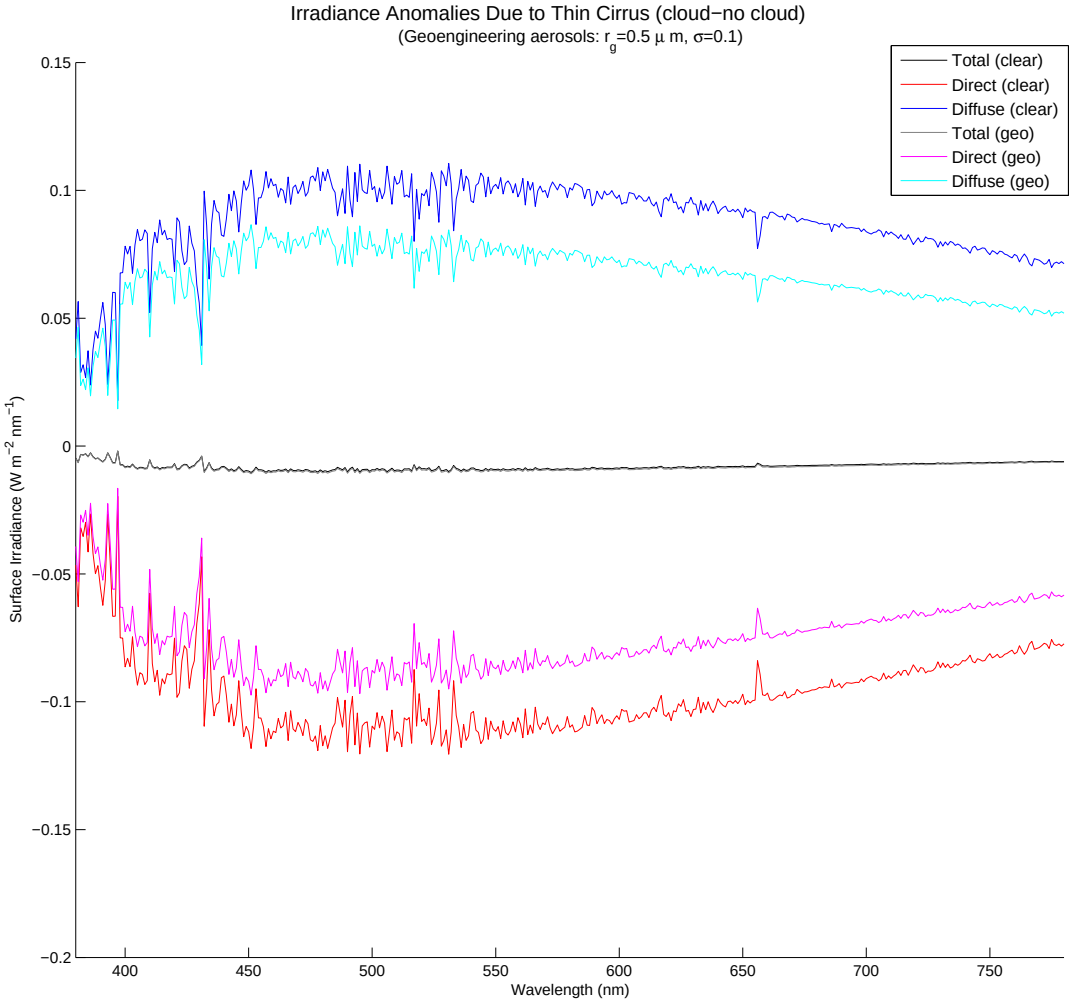


Figure 1: Geoengineering ($r_g$=0.5 $mu$m, $\sigma = 0.1$) and clear sky differences when optically thin cirrus clouds are included in the simulations. All values plotted are for simulations with clouds included minus simulations with no clouds. Specifications for cirrus clouds are in Supplementary Section 4.

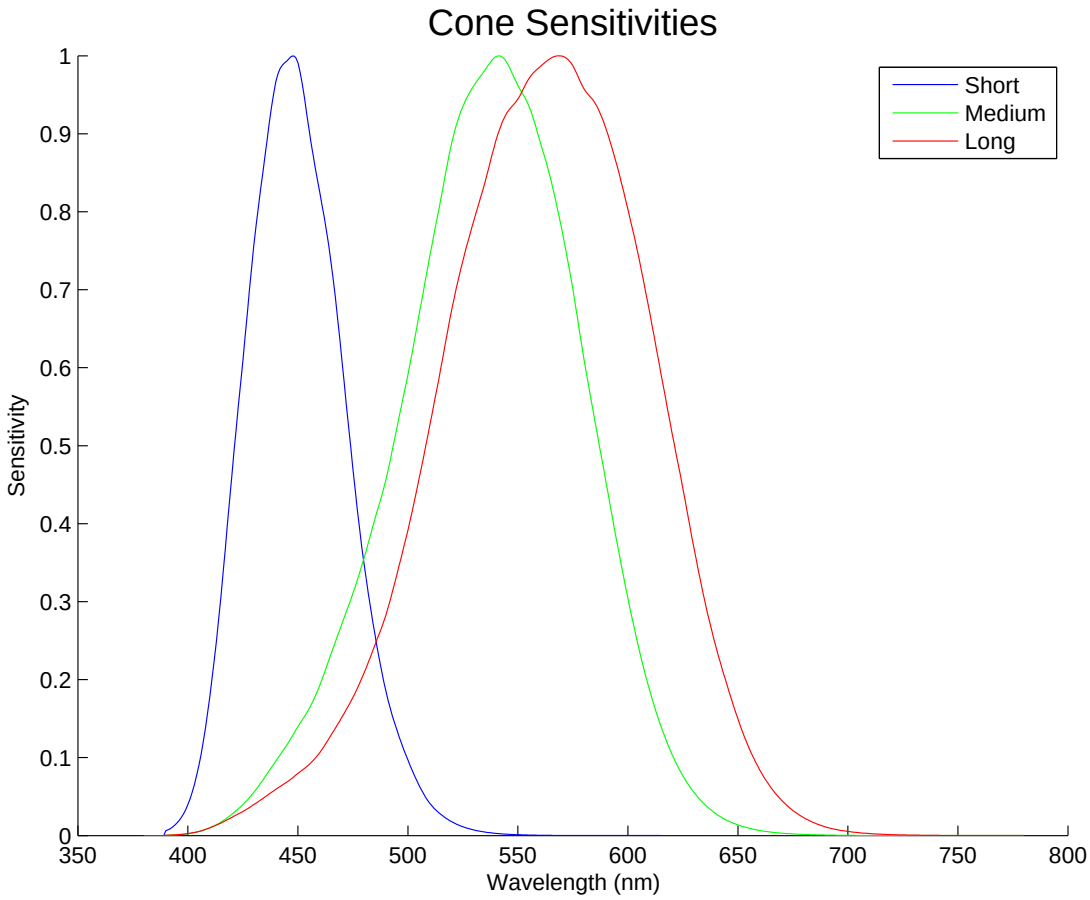


Figure 2: Average cone sensitivities used in the calculations of metameric matches (*19*). Values were obtained from http://cvrl.ioo.ucl.ac.uk. Sensitivities are shown for cones sensitive to short, medium, and long wavelengths.

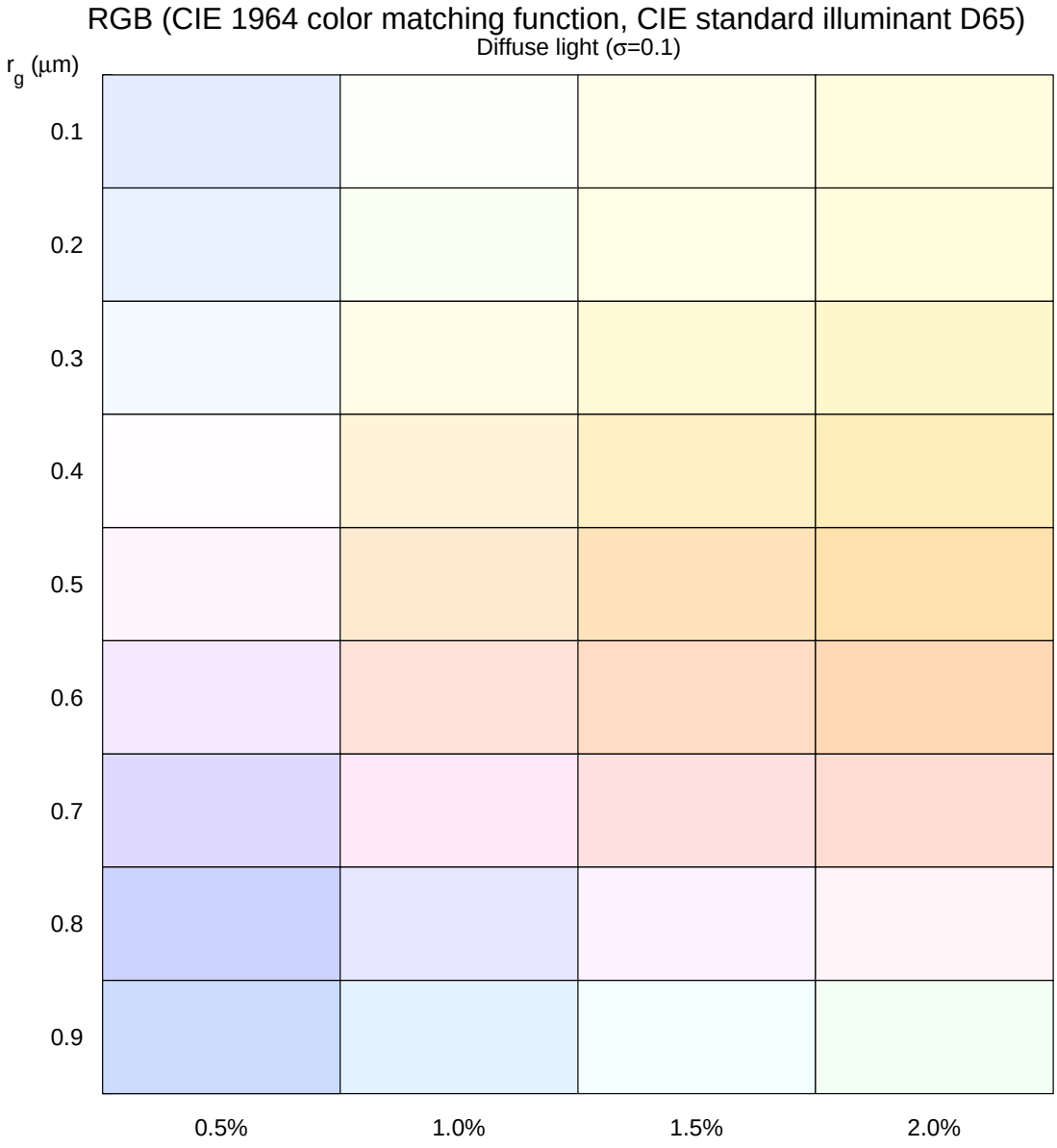


Figure 3: Color swatches of sky color from geoengineering as represented in RGB color space (one of four). To convert the diffuse light spectrum, the CIE 1964 color matching function was used (*20*), with a specified white point corresponding to the CIE standard illuminant D65, or a color temperature of 6504 K (*21*).

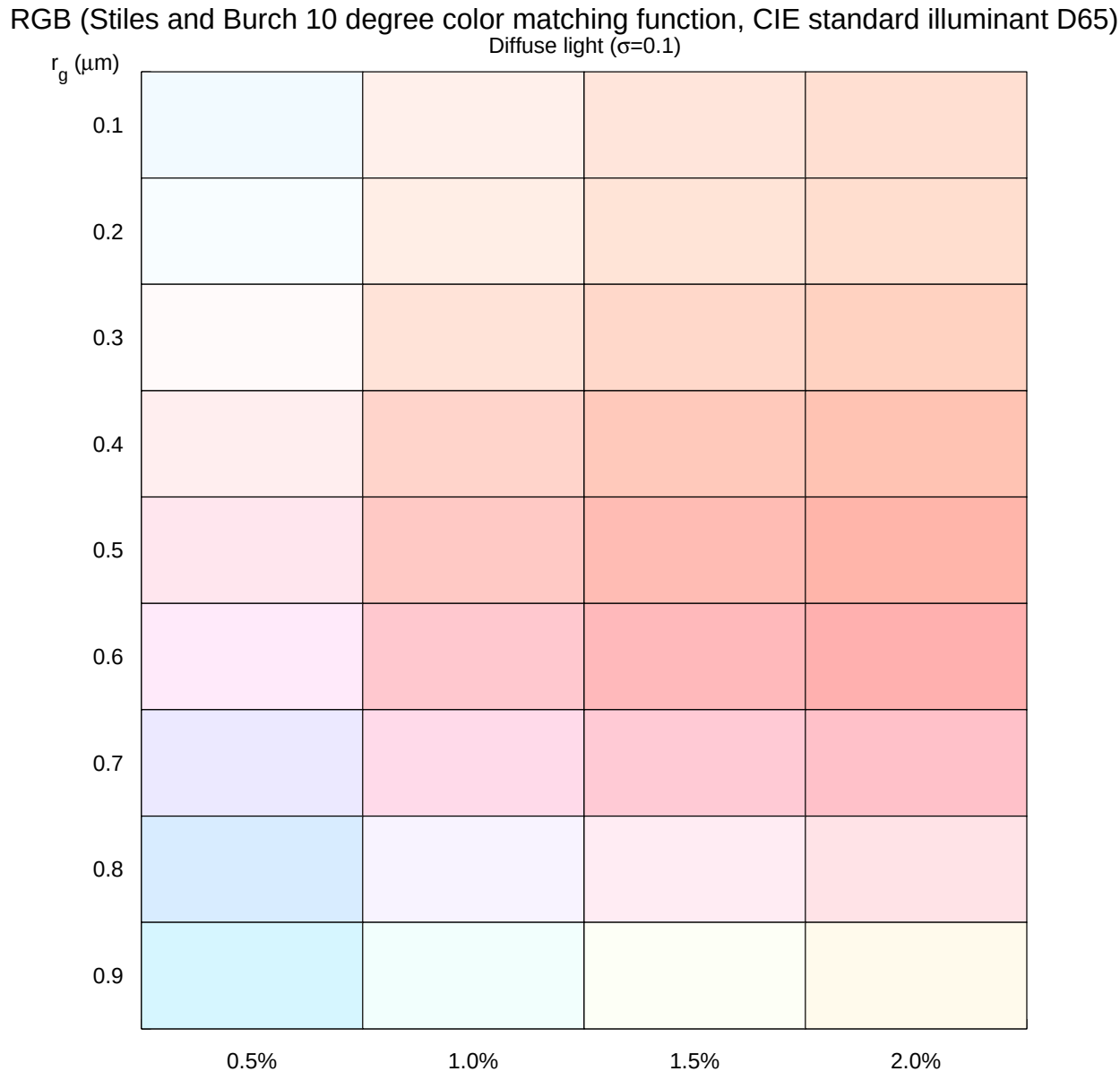


Figure 4: Color swatches of sky color from geoengineering as represented in RGB color space (two of four). To convert the diffuse light spectrum, the Stiles and Burch 10 degree color matching function was used (*22*), with a specified white point corresponding to the CIE standard illuminant D65, or a color temperature of 6504 K (*21*).

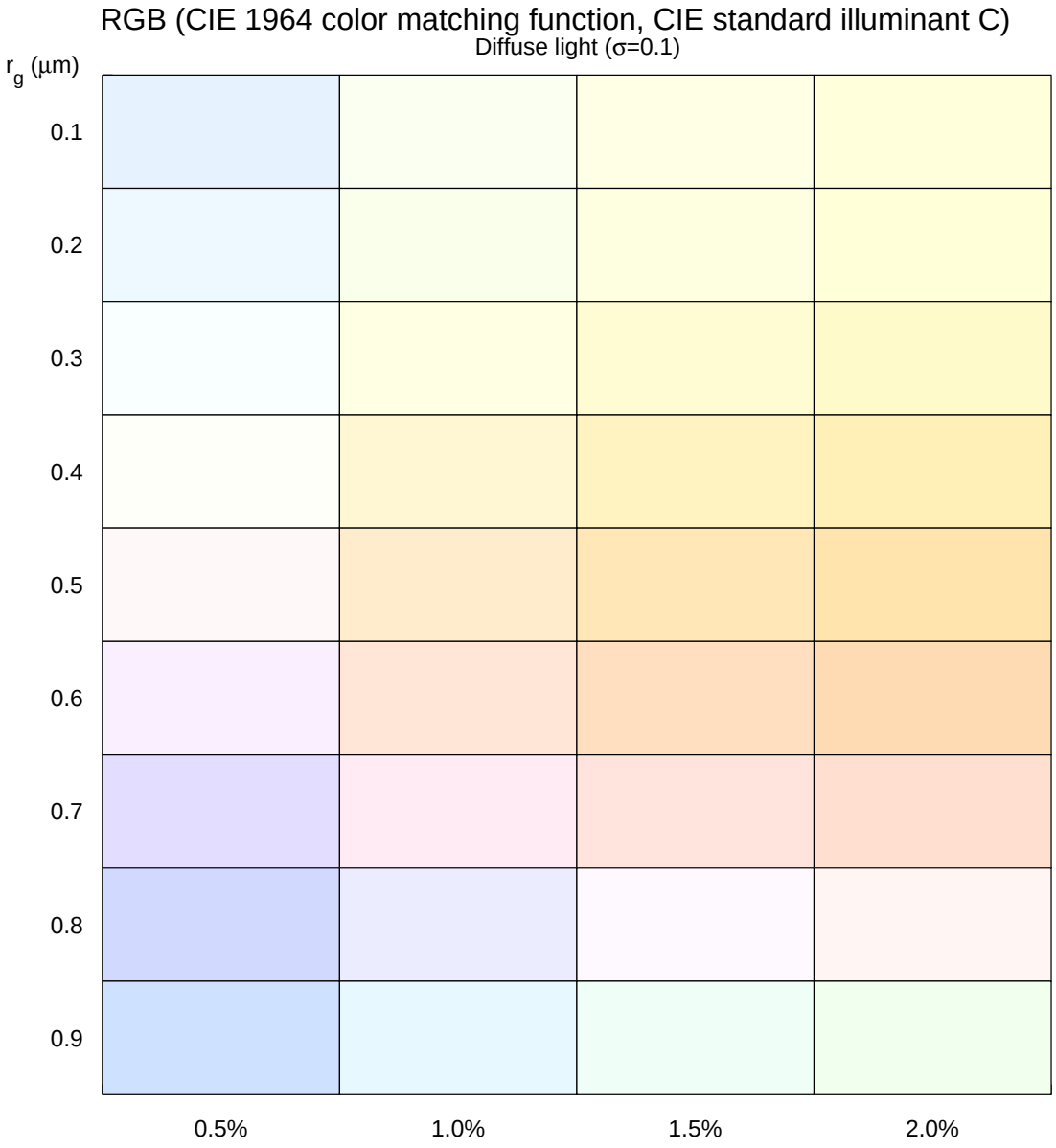


Figure 5: Color swatches of sky color from geoengineering as represented in RGB color space (three of four). To convert the diffuse light spectrum, the CIE 1964 color matching function was used (*20*), with a specified white point corresponding to the CIE standard illuminant C, or a color temperature of 6774 K (*21*).

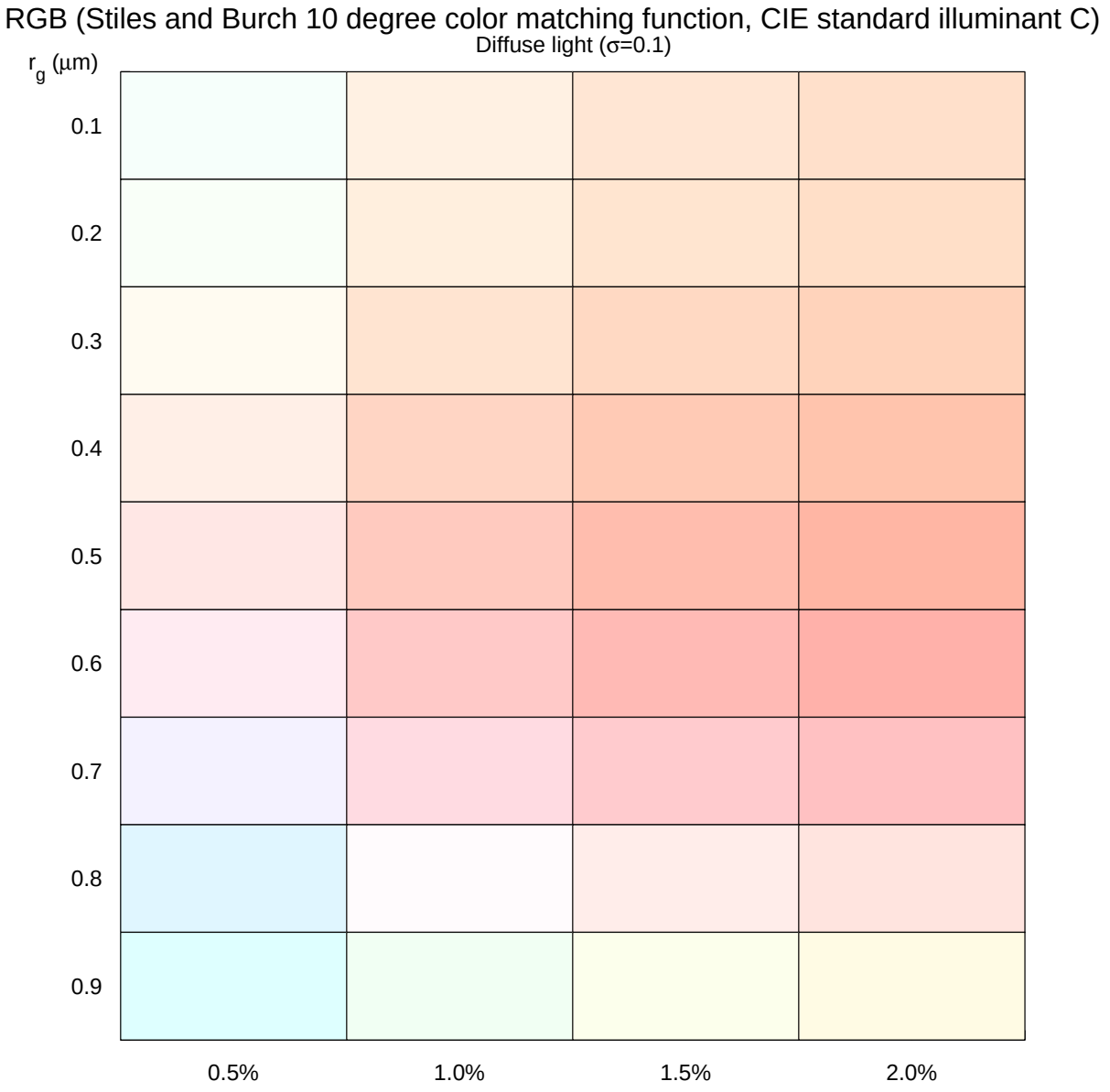


Figure 6: Color swatches of sky color from geoengineering as represented in RGB color space (four of four). To convert the diffuse light spectrum, the Stiles and Burch 10 degree color matching function was used (*22*), with a specified white point corresponding to the CIE standard illuminant C, or a color temperature of 6774 K (*21*).